JOURNAL OF PROPULSION AND POWER
Vol. 10, No. 1, Jan.–Feb. 1994

Numerical Study of Low-Pressure Concept for Nuclear Thermal Rockets

Suk C. Kim*
Sverdrup Technology, Inc., Brook Park, Ohio 44142
and
Robert M. Stubbs†
NASA Lewis Research Center, Cleveland, Ohio 44135

The flowfields and performance of low-pressure nuclear thermal rockets, which utilize nuclear fission energy and use hydrogen as a propellant, are studied by solving the Navier-Stokes equations and the species equations. A finite-rate chemistry model is used in the species equations and the turbulence is simulated by the modified Baldwin-Lomax turbulence model. The thrust level of the rocket for the present study is about 5000 lbf, and the length and exit radius of the nozzles are fixed to be 5.0 and 1.3 m, respectively. As the chamber pressure is varied, the throat areas of the various nozzles are adjusted accordingly to maintain approximately the same thrust level. The area ratio of the nozzle ranges from 4 for the chamber pressure of 0.1 atm to 240 for the chamber pressure of 6 atm. The calculated results for the chamber temperatures of 3200 and 4000 K with a chamber pressure range of 0.1–6 atm are presented as Mach number and static temperature contours, centerline variations of Mach number and static temperature, and exit profiles of Mach number and axial velocity. The vacuum specific impulse and thrust from the present calculations are compared with those from the one-dimensional, inviscid equilibrium and frozen flow code.

Nomenclature

A = area
A^+ = van Driest's damping constant
D_{im} = effective binary diffusivity of species i in the gas mixture
e = total internal energy
F, G = inviscid fluxes
F_v, G_v = viscous fluxes
h_i = enthalpy of species i
k = thermal conductivity
M = third body
p = pressure
q = heat flux
S = source term
T = temperature
t = time
u = axial velocity
$\bar{u}_i$ = axial diffusion velocity of species i
v = radial velocity
$\bar{v}_i$ = radial diffusion velocity of species i
$\dot{w}$ = chemical source term of species i
x, r, θ = cylindrical coordinates
Y_i = mass fraction of species i
μ = total viscosity, $\mu_l + \mu_t$
ρ = density
σ = normal stress
τ = shear stress

Subscripts
c = chamber or stagnation
e = exit
i = species, $i = 1$: H_2 and $i = 2$: H
t = throat
w = wall

Received May 4, 1992; revision received Feb. 26, 1993; accepted for publication June 23, 1993. This paper is declared a work of the U.S. Government and is not subject to copyright protection in the United States.

*Senior Research Engineer, Lewis Research Center Group, 2001 Aerospace Parkway. Member AIAA.
†Chief, Computational Method for Space Branch, Internal Fluid Mechanics Division, MS 5-11, 21000 Brookpark Road. Member AIAA.

Introduction

THE recent interest in missions to Mars has resulted in several space propulsion concepts which utilize nuclear fission energy and use hydrogen as a propellant. One of the concepts is the low-pressure nuclear thermal rocket which is designed to operate at low chamber pressure and high chamber temperature.[1–3] For an equilibrium expansion of high-temperature hydrogen gas through a converging-diverging nozzle with given area ratio and chamber temperature, the specific impulse increases as the chamber pressure decreases because of the dissociation and recombination of hydrogen molecules and atoms. The dissociation of hydrogen molecules into hydrogen atoms at the low chamber pressure results in a lower molecular weight and higher enthalpy inflow, which gives a higher specific impulse. The recombination of hydrogen atoms during the expansion through the converging-diverging nozzle which releases the recombination energy, but increases the molecular weight, can further increase specific impulse because the gain from the released recombination energy is greater than the penalty due to the higher molecular weight. But in a real nozzle operating at very low chamber pressure, the flow after the nozzle throat may not be in equilibrium but nearly frozen due to the low density of the flow, thus, the recombination effect can be small.

In an earlier study,[1] the performance of low-pressure nuclear rocket nozzles with an area ratio of 100 was investigated at various chamber pressures without considering the fact that the thrust and nozzle size can vary significantly with chamber pressure. For a nozzle with a given area ratio, as the chamber pressure decreases, the thrust decreases if the throat radius is constant. If the throat radius is increased to keep the thrust constant as the chamber pressure decreases, then the exit radius increases for a given area ratio nozzle. In Ref. 4 the performance of high-pressure nuclear thermal rockets was studied with the two-dimensional kinetics (TDK) code[5] by fixing the thrust and exit radius, but varying the nozzle length.

Because the components of the nuclear thermal rocket will be transported to low Earth orbit (LEO) and assembled there, it is more useful to investigate nozzles of the same maximum size and thrust level. To study the performance of low-pressure nuclear thermal rockets under those constraints, the present study holds the nozzle exit radius, length, and thrust constant as the chamber pressure is varied. Calculations are made for chamber temperatures of 3200 K, which can be achieved in the near future, and 4000 K, which needs advanced fuel elements and materials, with a chamber pressure range of 0.1–6 atm. A full Navier-Stokes code with finite-rate hydrogen chemistry, the RPLUS code, is used for the present study. The code, which was developed at NASA Lewis Research Center,[6] employs an implicit finite-volume, LU-SSOR scheme to solve the full Navier-Stokes equations and the species equations in a coupled manner, and has been previously used to calculate H_2/O_2 thruster flowfields,[7,8] high area ratio H_2/O_2 orbital transfer vehicle performance,[9] and nuclear thermal rocket flowfields.[10]

Nozzle Geometry

To study the effect of low chamber pressure on the performance of a nuclear thermal rocket at a given thrust level, a reference nozzle is selected to have approximately the same thrust and exit radius as those of the nozzle studied at INEL.[2] The chamber pressure and area ratio of the reference nozzle are selected to be 6 atm and 240, respectively. The chamber temperature is fixed to be 3200 K and the thrust level is assumed to be about 5000 lbf. The wall contour for the reference nozzle is obtained by running the Rao nozzle optimization program[11] for an area ratio of 240 by using the specific heat ratio and molecular weight from the output of the CET85 computer program[12] which calculates the chemical equilibrium compositions of hydrogen for given pressure and temperature. In running the Rao program, the radii of curvature upstream and downstream of the throat are assumed to be 1.5 times the throat radius. The output from the Rao program contains the nozzle wall contour nondimensionalized by the throat radius. The throat radius of the reference nozzle is selected to be 0.0837 m, which gives a vacuum thrust of about 5400 lbf for a one-dimensional inviscid frozen flow. The length after the throat and the exit radius of the reference nozzle are then 5.0215 and 1.2965 m, respectively. A nozzle of this size can be transported to LEO in the cargo bay of the Space Shuttle.

Once the reference nozzle geometry is determined, the nozzle length and exit radius for the other nozzles are fixed to those of the reference nozzle. Keeping the thrust constant for the other nozzles requires an iterative process because the exact value of thrust is not known until the calculations are made. Therefore, in the present study the area ratios are varied linearly with the reciprocal of the chamber pressure by adjusting the throat radii to obtain approximately the same vacuum thrust as that of the reference nozzle. The above adjustment of throat radius will give exactly the same thrust for the other nozzles if the flow is one-dimensional and inviscid and the gas is perfect, but in the present calculations it will give a different thrust for the other nozzles because the flow is viscous two-dimensional and the gas is not perfect. Once the area ratios are determined, the wall contours of the nozzles operating at various chamber pressures are obtained by running the Rao program. In the present study, the inlet radii of the nozzles are assumed to be 1.5 times the throat radii. Table 1 lists the area ratios and throat radii for the six nozzle test cases obtained by varying the chamber pressures. Figure 1 shows the geometry of the converging sections of the nozzles in the dimensionless coordinates where the physical coordinates are normalized by the throat radius r_t. As seen from this figure, the area ratios at the inlets of the nozzles are 2.25 and the throats are located at $x = 4r_t$, thus the length between the inlet and the throat ranges from 0.335 m for the chamber pressure of 6 atm to 2.59 m for the chamber pressure of 0.1 atm. The nozzle wall contours downstream of the throats are shown in Fig. 2. As shown in this figure, the nozzle lengths from the throats and the exit radii are all the same, but the throat radii and wall contours vary.

Table 1 Variation of throat radius with P_c

P_c, atm	r_t (m), throat radius	A_e/A_t, area ratio
0.1	0.6483	4
0.5	0.2899	20
1.0	0.2050	40
2.0	0.1450	80
4.0	0.1025	160
6.0	0.0837	240

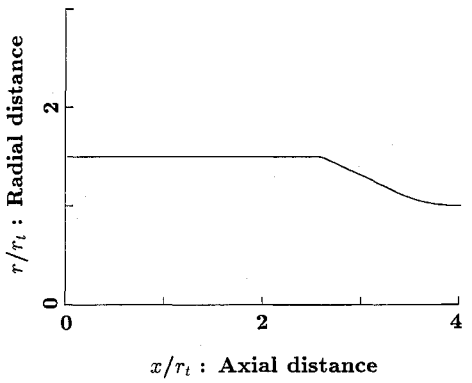

Fig. 1 Geometry of converging sections of the nozzles.

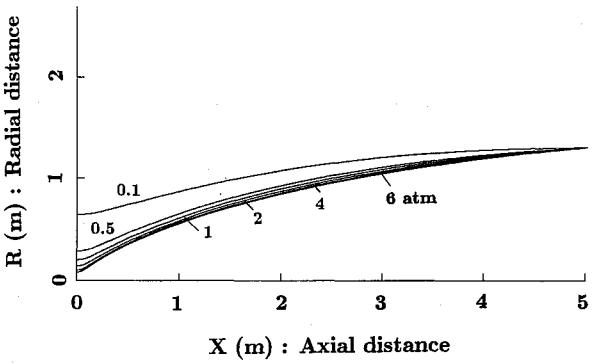

Fig. 2 Nozzle wall contours for various P_c.

Numerical Method

The Navier-Stokes equations and the species transport equations for axisymmetric flow can be written in the following form:

$$\frac{\partial Q}{\partial t} + \frac{\partial (F - F_v)}{\partial x} + \frac{1}{r}\frac{\partial [r(G - G_v)]}{\partial r} = S \qquad (1)$$

$$Q = \begin{bmatrix} \rho \\ \rho u \\ \rho v \\ \rho e \\ \rho Y_i \end{bmatrix} \quad F = \begin{bmatrix} \rho u \\ \rho u^2 + p \\ \rho uv \\ u(\rho e + p) \\ \rho u Y_i \end{bmatrix}$$

$$F_v = \begin{bmatrix} 0 \\ \sigma_{xx} \\ \tau_{rx} \\ u\sigma_{xx} + v\tau_{xr} - q_x \\ -\rho \bar{u}_i Y_i \end{bmatrix} \quad G = \begin{bmatrix} \rho v \\ \rho uv \\ \rho v^2 + p \\ v(\rho e + p) \\ \rho v Y_i \end{bmatrix}$$

$$G_v = \begin{bmatrix} 0 \\ \tau_{rx} \\ \sigma_{rr} \\ v\sigma_{rr} + u\tau_{xr} - q_r \\ -\rho \bar{v}_i Y_i \end{bmatrix} \quad S = \begin{bmatrix} 0 \\ 0 \\ -\tau_{\theta\theta}/r \\ 0 \\ \dot{w}_i \end{bmatrix}$$

where

$$\sigma_{xx} = 2\mu u_x - \tfrac{2}{3}\mu[u_x + v_r + (v/r)]$$

$$\sigma_{rr} = 2\mu v_r - \tfrac{2}{3}\mu[u_x + v_r + (v/r)]$$

$$\tau_{xr} = \tau_{rx} = \mu(u_r + v_x)$$

$$\tau_{\theta\theta} = \tfrac{4}{3}\mu(v/r) - \tfrac{2}{3}\mu(u_x + v_r) - p$$

$$q_x = -kT_x = \rho \sum_{i=1}^{2} h_i Y_i \tilde{u}_i$$

$$q_r = -kT_r + \rho \sum_{i=1}^{2} h_i Y_i \tilde{v}_i$$

$$Y_i \tilde{u}_i = -D_{im} Y_{ix}$$

$$Y_i \tilde{v}_i = -D_{im} Y_{ir}$$

The above Navier-Stokes and species transport equations are solved by the lower-upper symmetric successive over-relaxation (LU-SSOR) scheme[13] in the present study. The LU-SSOR scheme employs an implicit Newton iteration technique to solve the finite-volume approximation of the steady-state version of the governing equations. Even though the system of equations is formulated in a fully implicit and fully coupled manner, the LU-SSOR scheme requires only scalar diagonal inversion for the flow equations and diagonal block inversion for the species equations. The convergence of the Newton iteration method is assured by the diagonal dominance of the coefficient matrices of the LU-SSOR scheme. Detailed description of LU-SSOR scheme can be found in Refs. 6 and 13.

The following finite-rate chemistry model for the dissociation and recombination of hydrogen is used in the present study

$$H_2 + M \underset{k_b}{\overset{k_f}{\rightleftharpoons}} H + H + M \qquad (2)$$

where M is H and H_2, and $k_f = 2.20 \times 10^{11} e^{-48314.04/T}$ (m^3/kg mole s), and $k_b = 4.3848 \times 10^7 T^{0.0320618} e^{4166.86/T}$ (m^6/kg mole^2 s).

The specific heat, thermal conductivity, and viscosity of each species are given as fourth-order polynomials of temperature, and the coefficients of these polynomials are valid up to a temperature of 6000 K. The specific heat of the gas mixture is obtained by concentration weighting of each species, while the thermal conductivity and viscosity of the gas mixture are calculated from Wilke's mixing rule. The binary mass diffusivity between two species is obtained from the Chapman-Enskog theory in conjunction with the Lennard-Jones intermolecular potential function, and the diffusion of a species in a gas mixture is approximated by Fick's law.[6]

The turbulence model used in the present study is the Baldwin and Lomax model.[14] In the present study, the following modification on A^+ in the inner-layer model was made to include the pressure gradient effect[15]

$$A^+ = \frac{25}{30.175p^+ + 1.0} \qquad (3)$$

where

$$p^+ = \frac{\mu_w \left(\frac{dp}{dx}\right)}{\rho_w^{0.5} \tau_w^{1.5}}$$

Using the above modification, which gives a very large value of A^+ when there is a strong favorable pressure gradient, the relaminarization of the turbulent boundary layer can be predicted because the viscous sublayer overwhelms the entire boundary layer when the value of A^+ is very large. The effect of the above modification on the rocket nozzle performance can be found in Ref. 9.

Inflow and Boundary Conditions

In the present study, it is assumed that the flow is in chemical equilibrium and the inflow total enthalpy and total pressure are constant at the nozzle inlet where the area ratio is 2.25. For a given total pressure and temperature, the mass fractions of hydrogen atom and molecule at the inlet of the nozzle are obtained by running the CET85 code for an area ratio of 2.25, then they are assumed to be fixed. The inlet radial velocity is assumed to be zero and the inlet axial velocity is obtained by extrapolation from the interior, then the static temperature at the inlet is obtained from the inflow total enthalpy and the inlet axial velocity. The static pressure and density at the inlet are obtained from the isentropic relation and the equation of state, respectively.

At the exit of the nozzle where the flow is mostly supersonic, all dependent variables are extrapolated from the interior. The wall is assumed to be adiabatic and the no-slip condition is used at the wall. At the axis of symmetry, the radial velocity and the radial derivatives of the other dependent variables are set to be zero.

Results and Discussion

To study the effect of grid refinement on the performance values, calculations were made for the reference nozzle with both 240 × 60 and 480 × 120 grids. The results show that the differences in specific impulse and mass flow-rate between the solutions using the above two grids are 0.073 and 0.048%, respectively. Therefore, the calculations were made with a

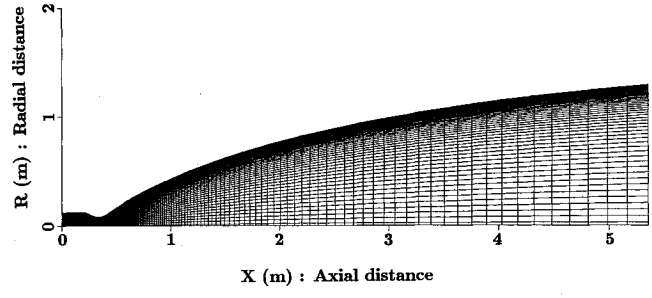

Fig. 3 Computational grid for the reference nozzle (P_c = 6 atm and A_e/A_t = 240).

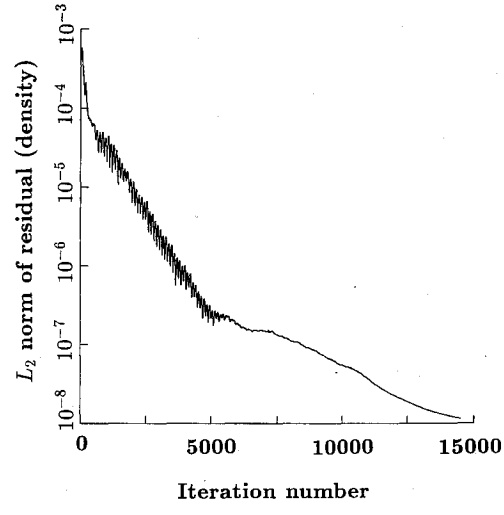

Fig. 4 Convergence history for the reference nozzle.

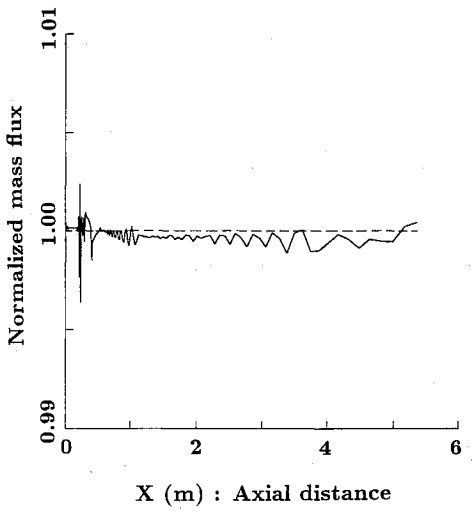

Fig. 5 Normalized mass flux variation with x for the reference nozzle.

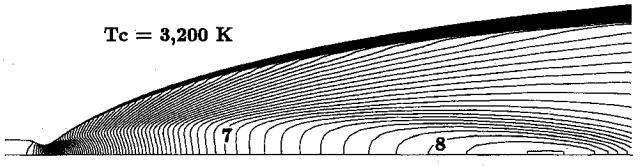

Fig. 6 Mach number contours of the reference nozzle (T_c = 3200 K).

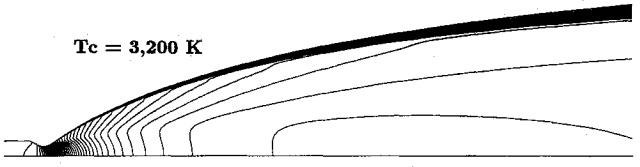

Fig. 7 Static temperature contours of the reference nozzle (T_c = 3200 K).

240 × 60 grid, which is adequate for the present performance study. Figure 3 shows the grid for the reference nozzle (A_e/A_t = 240 and P_c = 6 atm). As shown in this figure, a very small uniform axial grid size is used from the inlet to some distance downstream of the throat, after which the grid spacing increases. The radial grid size becomes finer near the wall.

Calculations were made for the chamber temperature of 3200 K and P_c = 0.1, 0.5, 1.0, 2.0, 4.0, 6.0 atm with the nozzle wall contours shown in Fig. 2. Figure 4 shows the convergence history for the reference nozzle. As seen from this figure, the density residual is reduced by four and a half orders of magnitude in 14,000 iterations. The calculated mass fluxes at various axial distances for the reference nozzle are normalized by the mass flux at the nozzle inlet and shown in Fig. 5. As shown in this figure, the overall error in mass conservation never exceeds plus or minus 0.4%, which is adequate for most engineering estimates.

Figure 6 shows the Mach number contours from the present calculations for the reference nozzle whose area ratio and chamber pressure are 240 and 6 atm, respectively. As seen from this figure, the inflow with a Mach number of about 0.27 rapidly accelerates through the converging-diverging nozzle to become supersonic. The boundary-layer development along the nozzle wall can be seen from the Mach number contours. Due to the very rapid expansion just downstream of the nozzle throat and subsequent more gradual expansion far downstream, compression waves are formed near the inflection point of the diverging section of the nozzle and strike the centerline near the exit of the nozzle as seen in Fig. 6. Figure 7 shows the static temperature contours from the present calculations for the reference nozzle. Both the boundary-layer development along the nozzle wall and compression waves are again visible in this figure. The static temperature of the flow at the inlet is about 3200 K and it reaches about 450 K at the exit.

Figures 8 and 9 show the Mach number and static temperature variations along the centerlines for various cases. In plotting these figures, the axial coordinates for the various nozzles are adjusted so that the throats are located at x = 1.62 m by either extending or shortening the lengths of constant area sections of the nozzle inlets. As seen from these figures, the Mach number increases while the static temperature decreases along the centerline until the compression waves strike the centerline. The maximum centerline Mach number is observed not at the nozzle exit, but at the axial station just before the location where the compression wave strikes the centerline, as seen from Fig. 8. The centerline Mach number increases with the chamber pressure due to the increase of the area ratio of the nozzle, and the largest centerline Mach number of about 8 is obtained for the nozzle with the chamber pressure of 6 atm whose area ratio is 240. The centerline static temperature variations show the same trends as the centerline Mach number as shown in Fig. 9.

Figure 10 shows the H_2 mass fraction variations along the centerlines for various cases and the H_2 mass fractions at the nozzle inlets are listed in Table 2. As seen from Table 2, H_2 mass fraction at the inlet decreases with decreasing chamber pressure because of the increase in H mass fraction due to the dissociation of H_2. As shown in Fig. 10, the centerline H_2 mass fraction for the chamber pressure of 0.1 atm is nearly constant along the nozzle due to the lack of recombination of hydrogen atoms in low-density flow, thus the flow is nearly frozen and there will be negligible specific impulse gain from

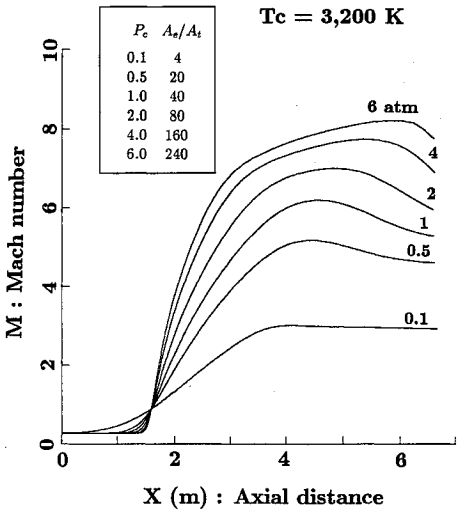

Fig. 8 Axial variations of centerline Mach number with P_c.

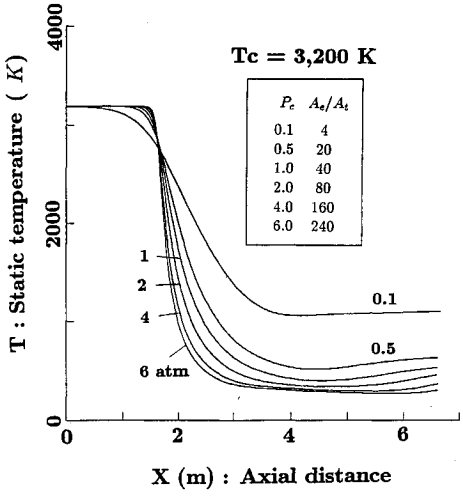

Fig. 9 Axial variations of centerline static temperature with P_c.

Table 2 Inflow H_2 mass fractions at various T_c and P_c

P_c, atm	H_2 mass fraction, T_c = 3200 K	H_2 mass fraction, T_c = 4000 K
0.1	0.59859	0.07496
0.5	0.80823	0.25787
1.0	0.86348	0.38266
2.0	0.90333	0.51454
4.0	0.93176	0.63459
6.0	0.94440	0.69492

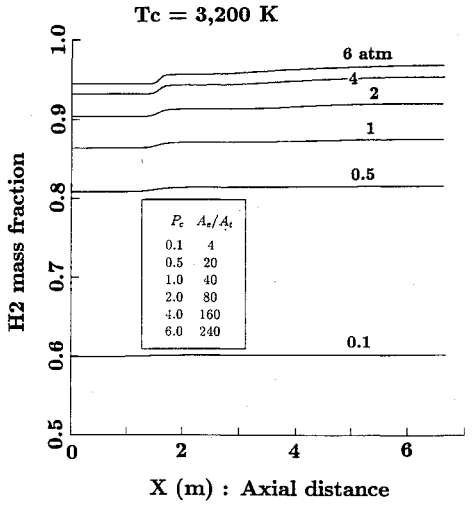

Fig. 10 Axial variations of centerline H_2 mass fraction with P_c.

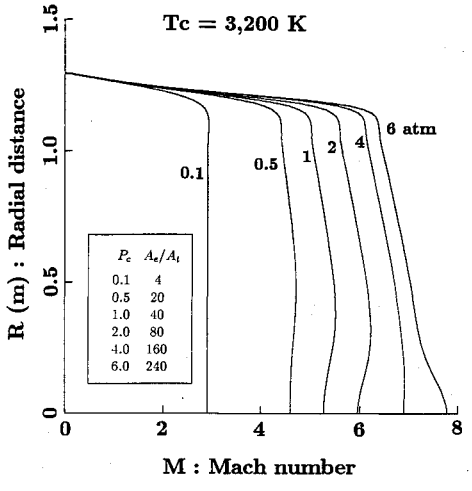

Fig. 11 Radial variations of exit Mach number with P_c.

the recombination. The centerline H_2 mass fraction for the chamber pressure of 6 atm changes noticeably near the nozzle throat because of the relatively high density of the flow which provides more opportunities for recombination of the hydrogen atoms.

Figure 11 shows the Mach number profiles at the exits of the nozzles for various chamber pressures. The nozzle wall boundary layers can be observed from this figure. It can be seen that the exit Mach number is nearly uniform. The large differences in the exit Mach number among the various nozzles are mainly due to the area ratio change which varies from 4 for the chamber pressure of 0.1 atm to 240 for the chamber pressure of 6 atm. Figure 12 shows the axial velocity profiles at the exits of the nozzles for various chamber pressures. As seen from this figure, the axial velocity is nearly uniform and it increases with the chamber pressure. The largest axial velocity of 10,400 m/s is obtained for the nozzle with the chamber pressure of 6 atm and the smallest axial velocity of 9000 m/s

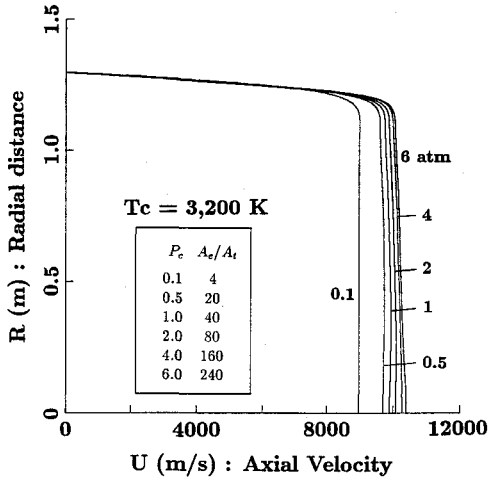

Fig. 12 Radial variations of axial velocity at the exit with P_c.

is obtained for the nozzle with the chamber pressure of 0.1 atm.

In the present study, the unit Reynolds number based on the flow properties at the inlet of the nozzle operating at the chamber temperature of 3200 K ranges from 1.58×10^4/m for the chamber pressure of 0.1 atm to 1.04×10^6/m for the chamber pressure of 6 atm. The calculated turbulent viscosity variations in the nozzle wall boundary layer indicate that by using Eq. (3) the relaminarization is predicted near the beginning of the converging sections of all six nozzles due to the very strong favorable pressure gradient. Even though the calculations were made with the assumption that the flow is turbulent, the calculated turbulent viscosity is much lower than the laminar viscosity in most parts of the nozzle, thus the flow is laminar-like.

To study the performance of the nozzle, the vacuum specific impulse and thrust are calculated from the exit profiles. There are four competing effects which affect the performance of the present nozzles: 1) dissociation of hydrogen molecules at low chamber pressure, which results in lower molecular weight and higher enthalpy inflow at the inlet, but requires higher energy input per unit mass; 2) recombination of hydrogen atoms downstream of the nozzle inlet which releases the recombination energy but increases the molecular weight downstream of the inlet; 3) area ratio of the nozzle which determines the expansion of the flow through the nozzle; and 4) Reynolds number of the flow which determines the viscous loss.

Effect 1 is favorable for the low-pressure nozzles if there is an unlimited energy source. The energy source of the nuclear rocket is the nuclear reactor which has an enormous power density, therefore, it is reasonable to assume that the nuclear reactor is an unlimited energy source in the present study. Effect 2, which is the recombination effect, is favorable for the low-pressure nozzles if appreciable recombination occurs at low pressure. The recombination of hydrogen atoms in the nozzle decreases with decreasing flow density, thus effect 2 is dependent on the chamber pressure. Unfortunately, for the nozzles with very low chamber pressure, the flow is nearly frozen in the nozzle and effect 2 is small. In the present study, effect 3 is favorable for the high-pressure nozzles because the area ratio increases with chamber pressure. The unit Reynolds number based on the flow properties at the inlet increases with increasing chamber pressure, thus effect 4 is also favorable for the high-pressure nozzles in the present study.

To study the effect of finite-rate chemistry on performance, calculations were also made for some of the present nozzles assuming that the flow is frozen from the nozzle inlet. Figure 13 shows the vacuum specific impulses from the present calculations using finite-rate chemistry and frozen chemistry

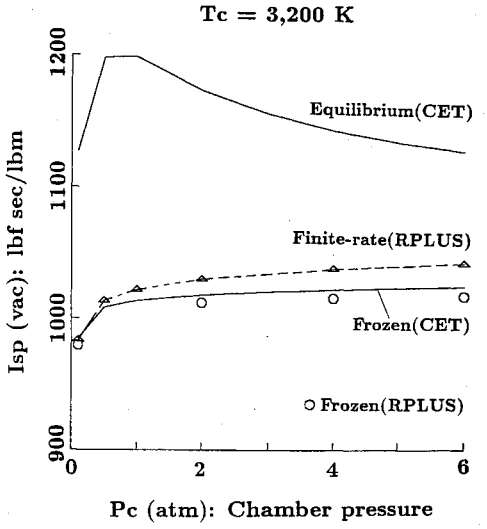

Fig. 13 Vacuum specific impulse vs P_c for T_c = 3200 K.

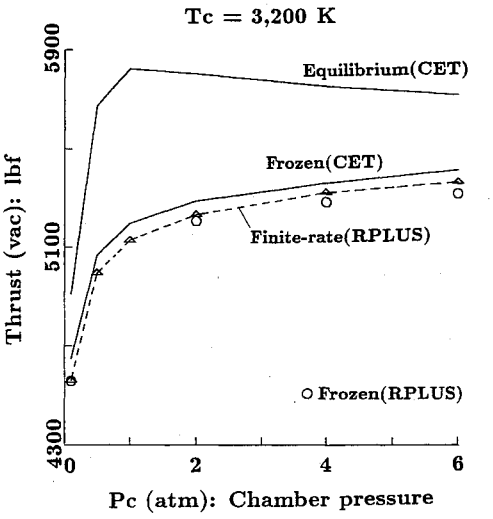

Fig. 14 Vacuum thrust vs P_c for T_c = 3200 K.

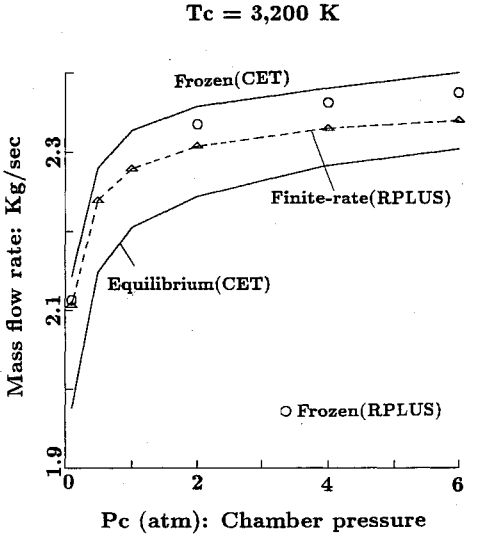

Fig. 15 Mass flow rate vs P_c for T_c = 3200 K.

compared with the values for the inviscid one-dimensional equilibrium and frozen flows from the CET85 code. In running the CET85 code for the frozen flow, it is assumed that the flow is frozen from the stagnation chamber. As seen from Fig. 13, the specific impulse for the equilibrium flow is significantly higher than that for the frozen flow due to the recombination of hydrogen atoms. For the frozen flow, the specific impulse increases with the chamber pressure because the area ratio effect is more significant than the dissociation effect in the pressure chamber. For the equilibrium flow, the specific impulse increases with decreases in the chamber pressure at higher chamber pressures because the dissociation and recombination effects are larger than the area ratio effect, but at very low chamber pressures where the area ratios are very small it decreases because the effect of area ratio becomes larger than the dissociation and recombination effects.

As shown in Fig. 13, the specific impulses from the present calculations with frozen chemistry are lower than the values for the frozen flow from the CET85 program for all cases. Even though there is some performance gain from the recombination between the stagnation chamber to the inlet in the present calculations with frozen chemistry because the flow is assumed to be in equilibrium at the inlet in the present study, this performance gain is smaller than the viscous and two-dimensional losses as seen from Fig. 13. The comparison between the specific impulses from the present calculations with finite-rate chemistry and frozen chemistry shows that the specific impulse obtained using finite-rate chemistry is higher than that using frozen chemistry due to the performance gain from the recombination effect, and the difference increases slightly as the chamber pressure increases. The specific impulses from the present calculations with finite-rate chemistry are larger than the values for the frozen flow from the CET85 code when the chamber pressure is larger than 0.1 atm, because there is some recombination which has a larger effect on performance than the viscous and two-dimensional losses, but at very low chamber pressure where there is a larger viscous loss and the flow is nearly frozen, the specific impulse value from the present calculations is lower than that for the frozen flow from the CET85 code. The highest specific impulse of 1041 lbf-s/lbm is obtained at the highest chamber pressure, 6 atm.

Figure 14 shows the calculated vacuum thrusts from the present study with the values from the CET85 code. As seen from this figure, the calculated vacuum thrusts from the present study are less than those for the frozen and equilibrium flow from the CET85 code. The thrust decreases significantly with decreasing chamber pressure even though the throat area is linearly varied with the reciprocal of the chamber pressure for various cases as seen from Fig. 14. These significant variations of thrust are mainly due to the mass flow rate variations with chamber pressure. Figure 15 shows the calculated mass flow rates from the present study with the values from the CET85 program for the inviscid one-dimensional equilibrium and frozen flows. The variation of mass flow rate with chamber pressure in Fig. 15 is due to the various degrees of dissociation of hydrogen molecule at various pressures which change the specific heat ratios and molecular weights of the flows at the inlets, thus the inflow density and velocity. The calculated mass flow rates from the present calculations are between those of the equilibrium and frozen flows as seen from Fig. 15.

Calculations were also made for the chamber temperature of 4000 K and P_c = 0.1, 0.5, 1.0, 2.0, 4.0, 6.0 atm with the nozzle geometries in Fig. 2. The vacuum specific impulses from the present calculations using the finite-rate chemistry are shown with those for the inviscid one-dimensional equilibrium and frozen flows from the CET85 program in Fig. 16. For the frozen flow, the specific impulse decreases with the chamber pressure when the chamber pressure is greater than 0.5 atm in contrast to the case of T_c = 3200 K. This is due to the fact that at higher chamber temperatures, the dissociation of hydrogen molecules in the pressure chamber plays an important role in improving performance of the low-pressure nozzle, overshadowing any performance benefits from the high area ratio of higher pressure nozzles. The specific impulses from the present calculations are nearly constant

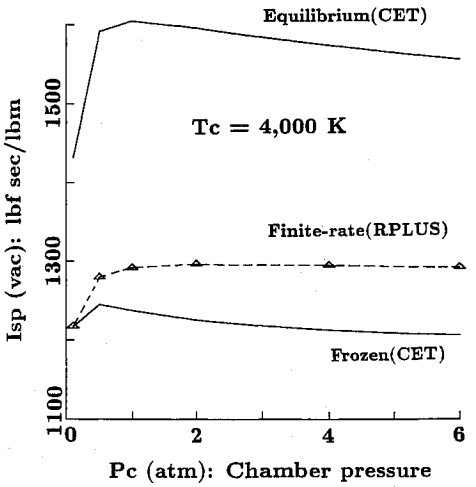

Fig. 16 Vacuum specific impulse vs P_c for T_c = 4000 K.

when the chamber pressure is greater than 1.0 atm in contrast to the case of T_c = 3200 K due to the recombination effect which increases the performance of high-pressure nozzles and the dissociation effect mentioned earlier for the frozen flow. The specific impulses from the present calculations do not follow the trend from the CET85 code for the frozen flow because the specific impulse gain from the recombination effect increases with the chamber pressure. The other trends are similar to those for the chamber temperature of 3200 K in Fig. 13, but the specific impulses are much larger than those for T_c = 3200 K as seen from this figure.

The low-pressure nuclear thermal rocket requires much more energy than the high-pressure nuclear thermal rocket with a comparable thrust, because considerable energy goes into dissociation of hydrogen molecules, but it is not a limitation for the nuclear rocket because of the enormous energy release in the nuclear reaction. The main limitation of the low-pressure nuclear thermal rocket for the high-thrust application is the size of the nozzle. To obtain the high thrust from the low-pressure rocket, the throat area should be increased, which results in an unrealistic exit radius for a moderate area ratio, thus the area ratio of the nozzle must be kept very low, which reduces specific impulse.

Conclusions

The flowfields and performance of low-pressure nuclear thermal rockets using hydrogen as a propellant were studied by solving the Navier-Stokes equations and the species equations simultaneously. A finite-rate hydrogen chemistry model is used in the species equations. The thrust level of the rocket for the present study is about 5000 lbf, and the length and exit radius of the nozzles are fixed to be 5.02 and 1.30 m, respectively. As the chamber pressure is varied, the throat areas of the various nozzles are adjusted accordingly to maintain approximately the same thrust level, thus the area ratio of the nozzles for the present study ranges from 4 for the chamber pressure of 0.1 atm to 240 for the chamber pressure of 6 atm. The nozzle wall contours for various chamber pressures are obtained by running the Rao nozzle optimization program. The flowfields for the chamber temperatures of 3200 and 4000 K with a chamber pressure range of 0.1–6 atm are calculated. The calculated results show that the flow is nearly chemically frozen downstream of the throat for the low-pressure rocket nozzle, thus the effect of recombination of hydrogen atoms on the rocket performance is small. The highest vacuum specific impulse for the chamber temperature of 3200 K is obtained at the chamber pressure of 6 atm. The vacuum thrust from the present calculations ranges from 4560 lbf for the nozzle with the chamber pressure of 0.1 atm to 5360 lbf for the nozzle with the chamber pressure of 6 atm at the chamber temperature of 3200 K.

Acknowledgments

The work of S. C. Kim was supported by NASA Lewis Research Center under Contract NAS3-25266. This work was performed using the computational resources of the NASA Lewis Research Center.

References

[1]Ramsthaler, J. H., Leyse, C. F., Madsen, W. W., Newmann, J. E., and Schnitzler, B. C., "Low Pressure Radial Flow Nuclear Rocket Concept (LPNTR)," Nuclear Thermal Propulsion, NASA CP-10079, July 1990.

[2]Leyse, C. F., Ramsthaler, J. H., Culver, D. W., and Haloulakos, V. E., "Cost Effective Development of a Nuclear Thermal Rocket Engine (NTRE)," AIAA Paper 91-3583, Sept. 1991.

[3]Eddy, T. L., Allemeier, R. T., Grandy, J. D., and Wilson, G. C., "Hydrogen Recombination Experiments in C-D Nozzle," AIAA Paper 91-3579, Sept. 1991.

[4]Davidian, K. O., and Kacynski, K. J., "Analytical Study of Nozzle Performance for Nuclear Thermal Rocket," AIAA Paper 91-3578, Sept. 1991.

[5]Nickerson, G. R., Coats, D. E., and Bartz, J. L., "Engineering Programmings and Users Manual; Two-Dimensional Kinetic Reference Computer Program," NASA CR-152999, Dec. 1973.

[6]Shuen, J.-S., and Yoon, S., "Numerical Study of Chemically Reacting Flows Using a LU-SSOR Scheme," *AIAA Journal*, Vol. 27, No. 12, 1989, pp. 1752–1760.

[7]VanOverbeke, T. J., and Shuen, J.-S., "A Numerical Study of Chemically Reacting Flow in Nozzle," NASA TM-102135, July 1989.

[8]Kim, S. C., and VanOverbeke, T. J., "Performance and Flow Calculations of Gaseous H_2/O_2 Thruster," *Journal of Spacecraft and Rockets*, Vol. 28, No. 4, 1991, pp. 433–438.

[9]Kim, S. C., "Numerical Study of High-Area-Ratio H_2/O_2 Rocket Nozzles," AIAA Paper 91-2434, June 1991.

[10]Stubbs, R. M., Kim, S. C., and Benson, T. J., "Computational Fluid Dynamics Studies of Nuclear Rocket Performance," AIAA Paper 91-3577, Sept. 1991.

[11]Rao, G. V. R., "Exhaust Nozzle Contour for Optimum Thrust," *Jet Propulsion*, Vol. 28, June 1958, pp. 377–382.

[12]Gordon, S., and McBride, B. J., "Computer Program for Calculation of Complex Chemical Equilibrium Compositions, Rocket Performance, Incident and Reflected Shocks, and Chapman-Jouguet Detonations," NASA SP-273, March 1976.

[13]Yoon, S., and Jameson, A., "A LU-SSOR Scheme for the Euler and Navier-Stokes Equations," AIAA Paper 87-0600, Jan. 1987.

[14]Baldwin, B. S., and Lomax, H., "Thin Layer Approximation and Algebraic Model for Separated Turbulent Flows," AIAA Paper 78-0257, Jan. 1978.

[15]Kays, W. M., and Crawford, M. E., *Convective Heat and Mass Transfer*, McGraw-Hill, New York, 1980, pp. 182–184.